



ISSN 2347-3487

Rapidly Solidified Melt-spun Bi-Sn Ribbons: Surface Composition Issues

Tarek El Ashram^{1,2*}, Ana P. Carapeto³, Ana M. Botelho do Rego³

1- Physics Department, Faculty of Science, Port Said University, Port Said, Egypt.

2- Physics Department, Preparatory Year Deanship, Jazan University, Jazan, KSA.

*Corresponding Author e-mail: tnelashram@gmail.com

3- Centro de Química-Física Molecular and Institute of Nanoscience and Nanotechnology, Instituto Superior Técnico, University of Lisbon, Av. Rovisco Pais, 1049-001 Lisbon, Portugal.

ABSTRACT

Tin-bismuth alloy ribbons were produced using melt-spinning technique. The two main surfaces (in contact with the rotating wheel and exposed to the air) were characterized with Optical Microscopy and AFM, revealing that the surface exposed to the air is duller (due to a long-range heterogeneity) than the opposite surface. Also the XPS chemical composition revealed many differences between them both on the corrosion extension and on the total relative amounts of tin and bismuth. For instance, for the specific case of an alloy with a composition Bi-4 wt % Sn, the XPS atomic ratios Sn/Bi are 1.1 and 3.7 for the surface in contact with the rotating wheel and for the one exposed to air, respectively, showing, additionally, that a large segregation of tin at the surface exists (nominal ratio should be 0.073). This segregation was interpreted as the result of the electrochemical process yielding the corrosion products.

Keywords

oxides; intermetallic compounds; atomic force microscopy; photoelectron spectroscopy; surfaces

Academic Discipline And Sub-Disciplines

Materials Science; Surface Analysis

SUBJECT CLASSIFICATION

Surface Analysis, Alloys

TYPE (METHOD/APPROACH)

Experimental

Council for Innovative Research

Peer Review Research Publishing System

Journal: JOURNAL OF ADVANCES IN PHYSICS

Vol. 11, No. 5

www.cirjap.com, japeditor@gmail.com



1. INTRODUCTION

Metallic ribbons have many applications namely in stretchable electronics and sensing where their surfaces may play an important role because they will bind to other systems (bio-molecules in bio-sensors, as an example) and their surface properties (surface plasmon resonance, for instance) are important.

The rapidly solidified ribbons produced using the melt-spinning technique exhibit unusual properties due to their structure evolution. It has been established that rapid solidification can produce high strength structural materials for use in tools and bearing components, high temperature materials, corrosion-resistant materials, catalytic and storage materials and, finally, electrical and magnetic materials [1]. These properties actually depend on the structural changes produced in each particular case. For example, high mechanical strength is attainable in microcrystalline materials as a result of refined microstructure combined with increased alloying [2]. Rapid solidification can produce metastable (non-equilibrium) crystalline phases [3-5] and amorphous (non-crystalline) phases [3, 6, 7]. In addition, the structure of pure metals or alloys rapidly solidified from the melt is always unusual in some respect, even if the phases present have the same crystal structure as in the equilibrium pure metals or alloys. Recently, it was found that rapid solidification can produce semiconductors directly in some alloy systems [8-10].

Pure bismuth is known to be a semi-metal [11] being a very poor conductor since it has a small overlap between its filled and empty zones. This is the reason why its resistance decreases when melted, contrarily to the usual behavior in metals: the zone structure is partly destroyed when the lattice breaks up and induces some overlap between the filled and empty zones. However, it was shown [12] that the transition to semiconductor occurs, by quantum confinement, for linear dimensions of the order of ~ 30 nm. The doping with other elements, as tin, for instance, may decrease the electrical resistivity of bismuth [13]. Therefore, using rapid solidification and small additions of tin, the band structure of Bi may be changed; consequently its electrical conductivity may be increased. Moreover, melt-spun Bi/Sn alloys displayed the formation of intermetallic phase SnBi, which was not usually obtained under equilibrium conditions [14]. Among important applications of Bi-Sn alloys are the use as lead free solder [15] and as an electrode for Cd^{2+} detection [16].

Bi-Sn alloys rapidly solidified were studied by M. Kamal et al. [14] and it was found that these alloys exhibit zero and negative temperature coefficient of resistivity. It was also found that the resistivity of the ribbons of pure Bi changes with time at room temperature in a period of three days after preparation. It was shown that the oxide layers developed at the surfaces of rapidly solidified ribbons make a definite impact on the properties of the ribbons [17, 18].

X-ray photoelectron spectroscopy (XPS) is a very robust spectroscopy for qualitative (oxidation states, for instance) and quantitative characterization of elements at surfaces on the nanometer depth range [19-22]. It is, therefore, a very appropriate tool to study the native oxide layers in metallic materials. Additionally, through the charge accumulation on surface induced by photoelectron ejection, information about local surface conductivity, though qualitative in nature, may be obtained.

The development of an oxide layer during or after the preparation can affect the properties of rapidly solidified ribbons. Therefore, the aim of the present work is to characterize both morphologically and chemically the two surfaces (the surface next to the rotating wheel and the surface exposed to the air) of the Bi-4 wt.% Sn ribbons rapidly solidified by melt spinning technique. Optical microscopy and AFM were used for imaging the surfaces and XPS to determine their chemical state and composition.

2. EXPERIMENTAL PROCEDURE

The materials used in the present work were Sn and Bi fragments with a starting purity better than 99.99%. Ribbons were produced by the melt-spinning technique using a single copper roller (200 mm in diameter) [23, 24]. The angular velocity of the wheel was fixed at 2900 r.p.m. which corresponds to a linear speed of about $30.4 \text{ m}\cdot\text{s}^{-1}$. Required quantities of the used metals were weighted out for each charge and melted in a porcelain crucible. After the alloy was molten, the melt was thoroughly agitated using a graphite rod to promote the homogenization. The casting was done in air, the molten temperature was 773 K and the substrate was at room temperature. The specific composition Bi-4 wt.% Sn (corresponding to an atomic ratio $\text{Sn}/\text{Bi} = (4/118.7)/(96/209) = 6.8/93.2 = 7.3 \text{ at}\%$) was studied using all the characterization techniques. This particular composition was chosen to allow for a good signal to noise for the XPS Sn 3d region.

Multimode Scanning Probe Microscope set-up, driven by the Nanoscope IIIa electronics from Digital Instruments, was used to obtain AFM images in the intermittent contact mode at room conditions. AFM image profiles, roughness (RMS) and nano-object dimensions were obtained using the software WSxM (freeware) [25]. The optical microscope used to image the surfaces in the sub-millimeter scale was the one coupled to the AFM equipment.

For X-ray photoelectron spectroscopy measurements, a Kratos XSAM800 model was used. It was equipped with double anode, and operated in FAT mode, with a pass energy of 20 eV and a power of 120 W. The Al K_α non-monochromatic X-radiation (principal emission at 1486.6 eV) was used. Samples were mounted on the sample holder using double-side tape and were analyzed at room temperature, in UHV ($P \sim 10^{-7}$ Pa) and TOA set to 0° . Spectra were collected with a step of 0.1 eV, using a Kratos Vision software (version 2.2.9). X-ray source satellites and a Shirley background were subtracted. XPS Peak 4.1 [26] was used to fit each detailed region with pseudo-Voigt profiles (Gaussian-Lorentzian products). No flood gun was used for charge neutralization. Charge shift was corrected setting the spurious carbon contamination binding energy (BE) to 285 eV. For quantification purposes, sensitivity factors were 0.25 for C 1s, 0.66 for O 1s; 7.11 for Bi 4f and 3.4 for Sn 3d_{5/2}. XPS was performed on the two surfaces of the ribbon, the

surface in contact with the rotating wheel (herein named CS) and the surface exposed to the air during casting (herein named AS) before and after polishing with SiC polishing paper.

3. RESULTS AND DISCUSSION

3.1. Imaging

Ribbon surface in contact with the rotating wheel (CS) looked, at naked eye, very different from the surface in contact with air (AS): AS was significantly duller than CS as shown by both sides pictures displayed in Figure 1.

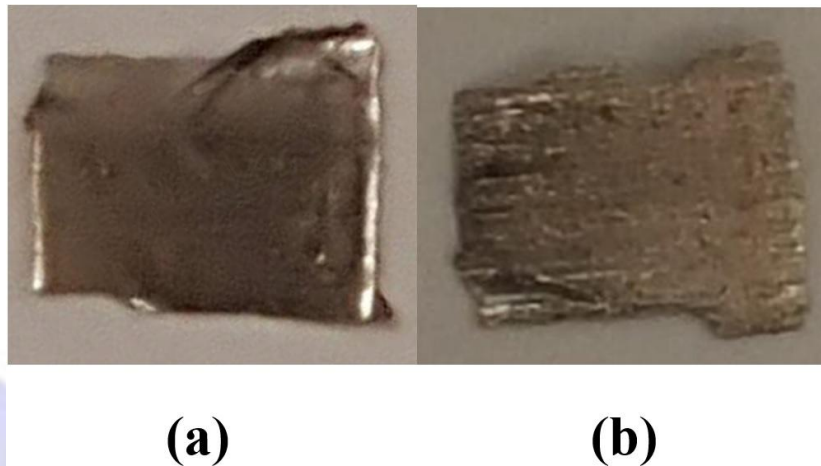


Fig. 1 Photograph of ribbon surfaces CS (a) and AS (b)

A more detailed view of these surfaces is shown in Figure 2 where optical microscopy images show that the surfaces have very different structures.

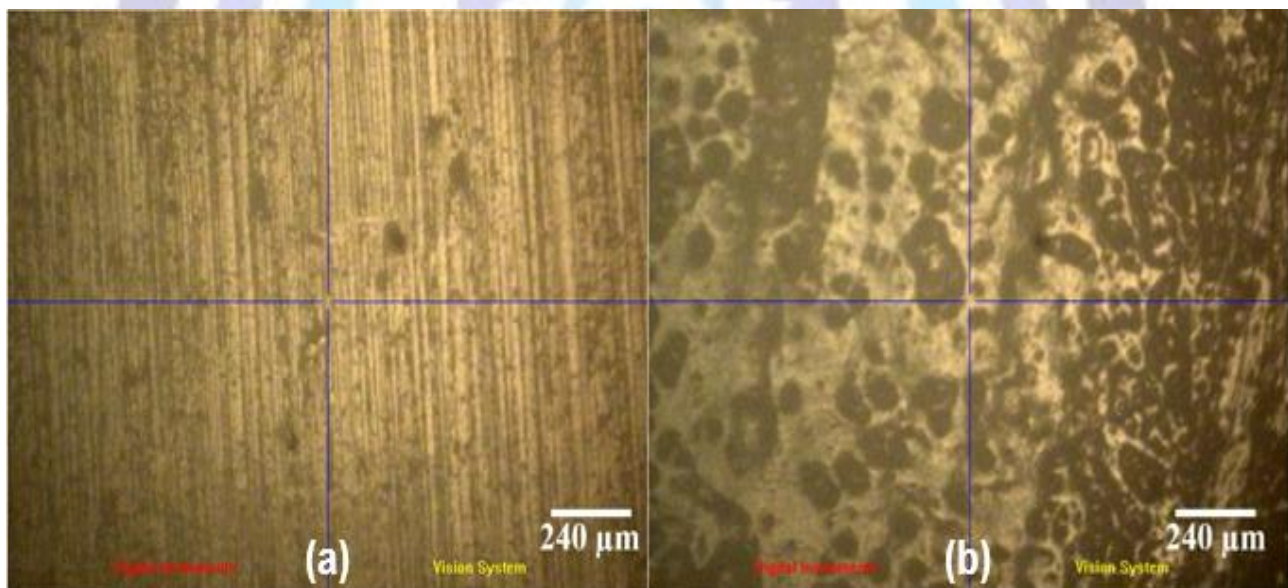


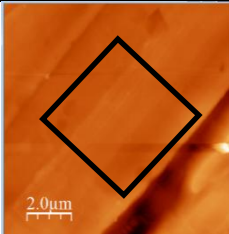
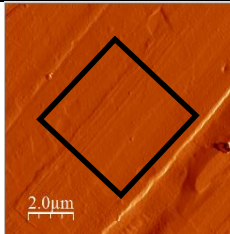
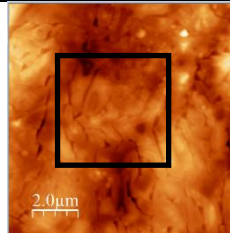
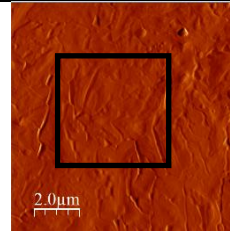
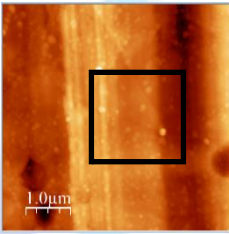
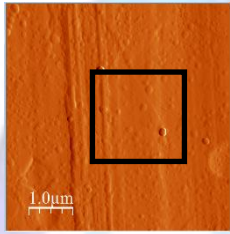
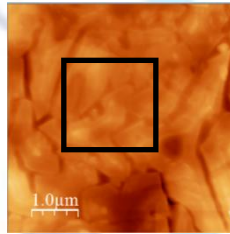
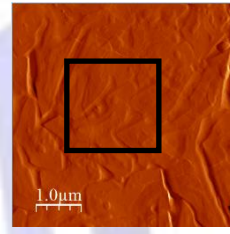
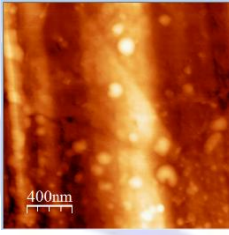
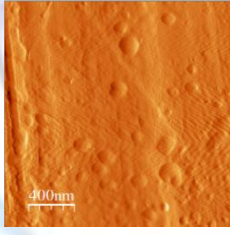
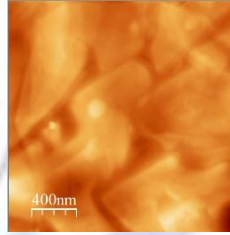
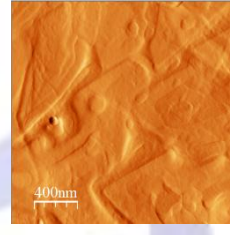
Fig. 2 Optical Microscopy images for CS (a) and AS (b) surfaces

A smaller scale imaging was also achieved using tapping mode AFM. Moreover, AFM allows to study local roughness, height profiles, comparing topographic images and phase contrast, among others. Table 1 shows AFM topography and phase contrast images.

Detailed images, especially the topographic AFM ones, show that the surface which macroscopically (Figure 1) seemed smoother (CS), presents a local higher roughness (higher RMS). Therefore, the local order is very different from the long-range order.

In addition, the simultaneously acquired phase images show the same features as the topographic images, which reveals homogeneity of mechanical/chemical properties of the surface.

Table 1. AFM topography and phase contrast images and respective RMS. Black squares correspond to the area swept in the next imaging scale.

AFM	CS		AS	
	Topography	Phase	Topography	Phase
10 × 10 μm ²				
Z-scale max (min=0)	1.00 μm	1.81 V	324.56 nm	1.76 V
RMS	82.21 nm		32.27 nm	
5 × 5 μm ²				
Z-scale max (min=0)	133.60 nm	1.11 V	257.52 nm	1.17 V
RMS	20.21 nm		25.36 nm	
2 × 2 μm ²				
Z-scale max (min=0)	37.42 nm	188.34 mV	98.75 nm	220.64 mV
RMS	7.17 nm		9.49 nm	

3.2. X-Ray Photoelectron Spectroscopy (XPS)

3.2.1. Chemical composition for as-received surfaces

Survey spectra revealed no elements other than Bi, Sn, O and C. The detailed regions of Bi 4f and Sn 3d for the as-received sample are shown in Figure 3; Table 2 gathers the main parameters for all the peaks fitted to the entire analyzed detailed XPS regions. Table 3 shows, in greater detail, the quantification results for metals (bismuth and tin).

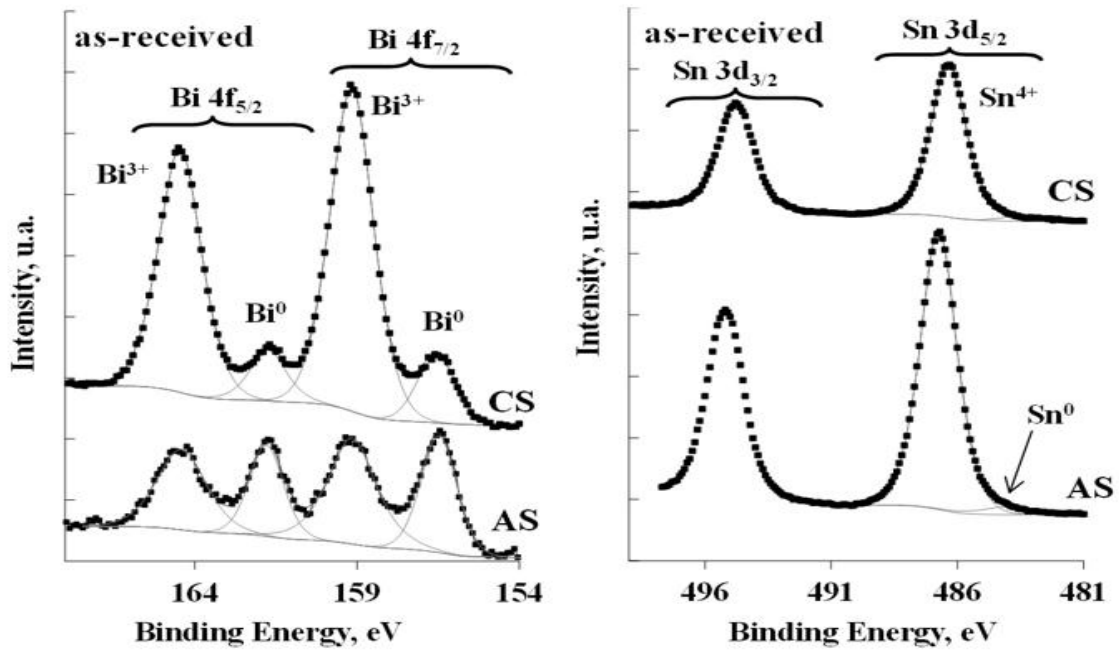


Fig. 3 XPS detailed spectra for Bi 4f and Sn 3d regions in both surfaces (CS and AS) for the as-received ribbons

Bismuth and tin were studied through their most intense regions Bi 4f and Sn 3d, respectively. The first one is composed of doublets Bi 4f_{7/2} / Bi 4f_{5/2} with a spin-orbit split of 5.3 ± 0.1 eV and the second one by doublets Sn 3d_{5/2} / Sn 3d_{3/2} with a spin-orbit split of 8.4 ± 0.1 eV. In both regions, for the two faces of the sample, two doublets existed as shown in Figure 3 and Table 2. They show that, in both surfaces of the ribbon (CS and AS), bismuth is in the elemental form Bi⁰ and Bi₂O₃ oxide, the relative amounts of each form being very different in both surfaces. The proportion of Bi₂O₃ is very large on the CS side while on the AS side, the proportion between Bi₂O₃ and Bi becomes much more balanced, as shown in Table 3. In what concerns tin, a very small component in the low BE side of both the Sn 3d_{3/2} and Sn 3d_{5/2} is detected and assigned to elemental Sn⁰ form. However, in both sample sides, the main component is assignable to Sn⁴⁺ in the form of SnO₂. This assignment is much more based on the stoichiometry to the existing oxygen than on the binding energy values for which a large dispersion of binding energy values exist in the literature for both the +2 and +4 oxidation states [27, 28]. The presence of carbon may be due to the adventitious carbon contamination or from graphite rod used to cause homogenization during preparation.

Table 2. Position (eV), atomic % and assignment of all the components fitted to XPS regions C 1s, O 1s, Bi 4f and Sn 3d_{5/2} for the as-received sample.

Peak	CS		AS		Assignment
	BE(eV)	at. %	BE(eV)	at. %	
C 1s1	285.0	33.7	285.0	25.6	Adventitious carbon
C 1s2	287.4	3.6	288.2	3.6	Carbonyl groups
C 1s3	289.0	2.8	290.4	2.1	Carbonate ion
O 1s1	530.0	22.9	530.6	30.7	Lattice oxygen
O 1s2	531.2	15.1	531.7	11.7	Lattice oxygen
O 1s3	533.1	2.1	532.7	2.3	Organic carbon
Bi 4f _{7/2} 1	156.5	0.8	156.5	1.3	Metallic Bi
Bi 4f _{7/2} 2	159.2	4.6	159.1	1.6	Bi ₂ O ₃
Bi 4f _{5/2} 1	161.7	0.6	161.8	1.0	Metallic Bi
Bi 4f _{5/2} 2	164.5	3.4	164.4	1.2	Bi ₂ O ₃
Sn 3d _{5/2} 1	483.8	0.5	484.5	0.4	Sn metal
Sn 3d _{5/2} 2	486.4	9.9	486.7	18.4	SnO ₂



The experimental BE and atomic % errors associated to peaks resolved in the spectrum (such as the two Bi 4f doublets), is, respectively ± 0.1 eV and less than $0.05 \times \text{at.}\%$. However, for fitted components, namely in the O 1s, or C 1s regions, the error is much larger and difficult to estimate.

Table 3. Relative XPS atomic percentages of bismuth and tin with different oxidation states for the as-received sample. Several atomic ratios are also included.

Phase	CS	AS
Metallic Bi	7.2	9.3
Bi ³⁺	40	12
Metallic Sn	2.7	1.7
Sn ⁴⁺	50	77
Total Sn/Bi	1.1	3.7
Sn metal/Bi metal	0.37	0.18
Sn ⁴⁺ /Bi ³⁺	1.2	6.4
Metallic "phase"/Oxidized "phase"	0.11	0.12

From Table 3, it is evident that the proportion of elements in the metallic phase to elements in the oxidized phase is very small on both surfaces i.e. the two sides of the ribbon are covered with thick oxide layers, thickness being of the order of magnitude of the escape length of photoelectrons here analyzed (a few nanometers). The proportion of SnO₂ on the AS surface is larger than Bi₂O₃ proportion on the CS surface. However, atomic percentages and ratios presented in Table 3 should be read with caution: they were computed assuming that the photoelectrons were coming from an uncovered infinite (in thickness) layer. Since the oxide layer is covering the metallic phase, two aspects should be taken into account:

i) For the metallic phase underneath the oxide layer, Sn 3d photoelectrons are more attenuated than the Bi 4f ones. As a matter of fact, the multiplying attenuation factor is given by $\exp(-l/\lambda_p)$, l being the overlayer thickness and λ_p the escape depth of the photoelectron which is usually taken as 0.9 times the inelastic mean free path (IMFP) [29]. On the other hand, the IMFP is an increasing function of the kinetic energy (KE). Since KE is given by $1486.6 - BE$, it is around 1330 eV and 1002 eV, respectively, for Bi 4f and Sn 3d photoelectrons; using the equation 1a from Tanuma et al. [30], we obtain for the IMFP (or λ_p), in SnO₂ oxide, the values of 18 Å (or 16 Å) and 22 Å (or 20 Å) respectively for Sn 3d and Bi 4f. Therefore, the intrinsic photoelectron intensities, before crossing the oxide layer, are multiplied by a smaller factor in the case of Sn 3d than in the case of Bi 4f. This suggests that Sn metal/Bi metal ratios in Table 3 are lower than the real ones (even if a large error may be associated to that ratio due to the very low intensity of Sn⁰ component and to the fact that it is in the tail of a much more intense peak) indicating that a large segregation of Sn at both surfaces exist.

ii) On the contrary, for the oxide overlayer, the atomic ratios may be over-estimated since, for a finite layer, photoelectron signal is proportional to $(1 - \exp(-l/\lambda_p))$ and, therefore, the Sn 3d signal is favored when compared to Bi 4f. However, the factor never exceeds 1.2 (or 0.8) and it would be so if l was much lower than λ_p [31] which, given the values of λ_p computed above, is not expected in this case.

Anyway, the total ratio Sn/Bi should not be (or just be slightly) affected and it is very clear that its value is much higher, in both surfaces, than the nominal one. Since the main components are the oxides resulting from the oxidation process, the explanation of this segregation should be discussed on the basis of the relative Standard Reduction Potentials at 25 °C, $E_{\text{Bi}^{3+}/\text{Bi}}^0 = +0.308$ V, $E_{\text{Sn}^{2+}/\text{Sn}}^0 = -0.14$ V and $E_{\text{Sn}^{4+}/\text{Sn}^{2+}}^0 = +0.15$ V. From these values it can be concluded that, thermodynamically, the tin in the presence of bismuth behaves as an anode and gets oxidized to Sn²⁺ and, eventually, to Sn⁴⁺. The charged species having higher mobility in humid media tend to easily segregate at the surface, the surface becoming very rich in (oxidized) Sn, specially in the surfaces where the oxidation conditions were more favorable. These should be exactly in the AS surface where the available O₂ is more abundant and, most probably, the humidity too. Once all the Sn reaching the surface is oxidized, bismuth also can be oxidized because of the existence of local electrochemical cells due to local atomic deformations (grain boundaries, for instance).

To try to have a clearer information about the metallic phase, especially from tin, the same surfaces, analyzed as-received, were polished as much as they could be (since they were brittle, they were just gently polished till the borders started to detach from the tape where they were fixed before the insertion in the XPS analysis chamber).

3.2.2. Chemical composition for polished surfaces

Figure 4 shows XPS spectra for Bi 4f and Sn 3d regions after polishing and Table 4 gathers the main parameters for all the fitted peaks.

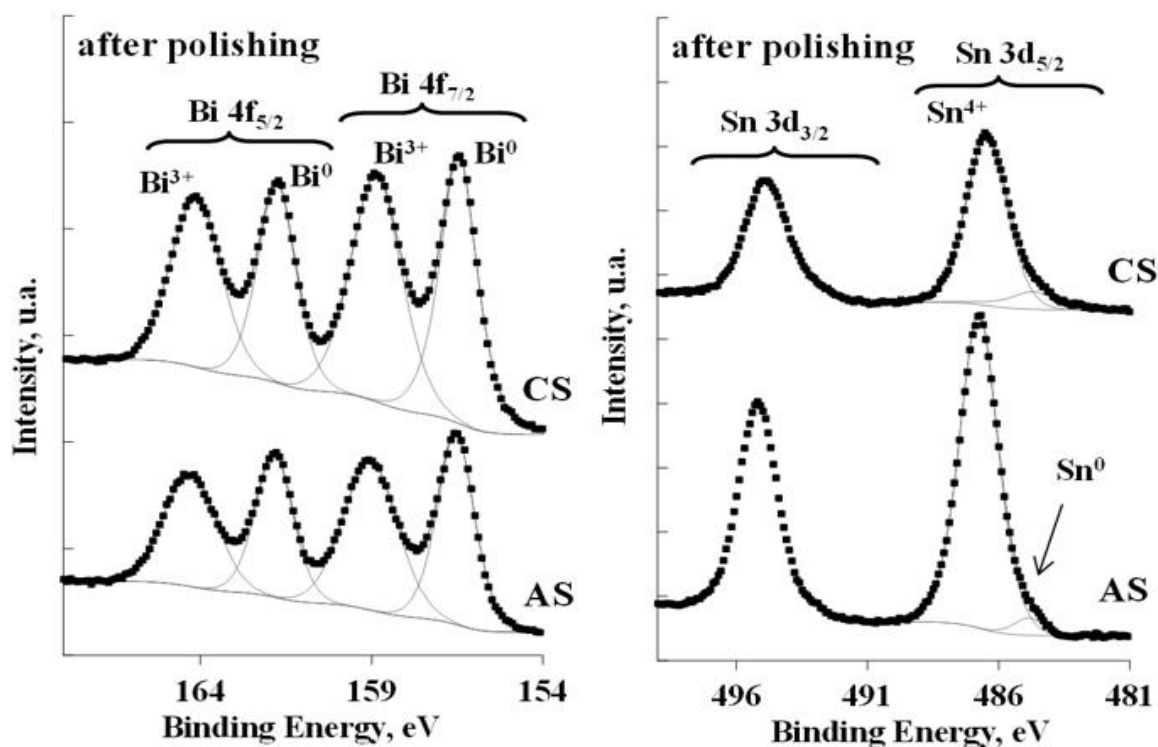


Fig. 4 XPS detailed spectra for Bi 4f and Sn 3d regions after polishing

Table 4. Position (eV), atomic % and assignment of all the components fitted to XPS regions C 1s, O 1s, Bi 4f and Sn 3d after polishing.

Peak	CS		AS		Assignment
	BE(eV)	at. %	BE(eV)	at. %	
C 1s1	285.0	44.6	285.0	34.5	Adventitious carbon
C 1s2	287.3	4.1	286.5	5.4	Carbonyl groups
C 1s3	289.4	3.7	288.8	3.5	Carbonate ion
O 1s1	530.2	14.3	530.6	19.8	Lattice oxygen
O 1s2	531.9	10.9	532.0	15.4	Lattice oxygen
O 1s3	533.7	3.3	533.8	2.5	Organic carbon
Bi 4f _{7/2} 1	156.5	2.7	156.5	1.6	Metallic Bi
Bi 4f _{7/2} 2	158.9	3.0	159.0	1.8	Bi ₂ O ₃
Bi 4f _{5/2} 1	161.8	2.0	161.8	1.2	Metallic Bi
Bi 4f _{5/2} 2	164.1	2.2	164.3	1.3	Bi ₂ O ₃
Sn 3d _{5/2} 1	484.7	1.1	484.9	0.6	Sn metal
Sn 3d _{5/2} 2	486.5	8.1	486.8	12.5	SnO ₂

After polishing, the relative amount of the metallic form increases, especially in the CS face, but keeps being a minor component as shown in Table 5.



Table 5. Relative XPS atomic percentages of bismuth and tin with different oxidation states after polishing. Several atomic ratios are also included.

Phase	CS	AS
Metallic Bi	25	15
Bi ³⁺	27	16
Metallic Sn	5.6	2.9
Sn ⁴⁺	43	66
Total Sn/Bi	0.9	2.2
Sn metal/Bi metal	0.23	0.20
Sn ⁴⁺ /Bi ³⁺	1.6	4.1
Metallic "phase"/Oxidized "phase"	0.44	0.22

3.2.3. XPS Full width at half maximum

The full width at half maximum (FWHM) of XPS peaks may also be very informative about the respective species. Table 6 contains their values for the peaks fitted to Bi and Sn XPS regions for both surfaces before and after polishing. A very evident feature is that, for bismuth, the metallic peak is much narrower than the oxidized one. It may be so for two reasons: i) the existence of mixture of oxides, since Bi may have two valence states (III and V); ii) the oxidized phase forming rougher and more amorphous aggregates than the metallic ones and, therefore, enlarging peaks.

Table 6. The full width (± 0.1 eV) at half maximum (FWHM) of XPS peaks.

Peak	As-received		After polishing	
	CS	AS	CS	AS
Bi 4f _{7/2} metallic	1.4	1.3	1.3	1.3
Bi 4f _{7/2} oxide	1.6	1.7	1.8	1.9
Bi 4f _{5/2} metallic	1.3	1.2	1.3	1.3
Bi 4f _{5/2} oxide	1.6	1.8	1.7	1.8
Sn 3d _{5/2} metallic	1.7	1.7	2.1	1.5
Sn 3d _{5/2} oxide	1.7	1.7	1.8	1.7

For Bi₂O₃, before polishing, the FWHM on the AS surface is greater than that on the CS surface. Additionally, an increase in FWHM after polishing is observed on both surfaces. These two facts point to the reason for peak broadening coming mainly from the amorphous structure of the oxides which likely becomes even more amorphous after the mechanical effect associated to the polishing action.

On the metallic phase, no such effect was expected. Values for metallic Sn seem to have been affected but that may be misleading: due to their very small intensity, especially in the as-received surfaces, their FWHM was constrained to be the same as the one for the oxide. In the polished surfaces, FWHM were allowed to fit freely. However, given their still low intensity, values obtained for the parameters of the low intensity peak have large errors.

3.2.4. XPS charge accumulation

An interesting point was found concerning the charge accumulation on the surface during XPS analysis: for as-received sample, the CS surface presented the smaller charge accumulation and the AS surface the largest one (inducing charge shifts of 0.6 and 7.1 eV, respectively). After polishing, the two surfaces present similar charge accumulation (charge shifts of 4.8 eV for the smooth face and 5.0 eV for the rough one).

**Table 7. Basic electrical properties for pure bismuth, pure tin and respective oxides, Bi₂O₃ and SnO₂.**

	Electrical resistivity (Ω m)	Classification	Energy gap (eV)
Pure Tin	11.7×10^{-8} (273 K) [32]	metal	_____
Pure bismuth	107×10^{-8} (273 K) [32]	semi-metal	_____
SnO ₂	$2.65 \times 10^{-4} - 3.57 \times 10^{-5}$ (150–200 °C) [33]	n-type semiconductor [34]	3.6 [35]
Bi ₂ O ₃	5×10^{13} (300 K) [36]	n-type/p-type semiconductor [37]	β -Bi ₂ O ₃ : 2.58, α -Bi ₂ O ₃ : 2.85 [38]

The charge accumulation occurs if the sample is insulator or has low electrical conductivity. This charge is eliminated if the sample is good electrical conductor. Now, the conductivity of the sample wheel surface (CS) is high due to the high proportion of Bi₂O₃ which has high ionic conductivity [39]. This, in turn, reduces the charge shift to 0.6 eV before polishing. On the other hand, the AS surface has low conductivity because it has high proportion of SnO₂ which is semiconducting with a lower energy gap than Bi₂O₃ [40], the charge shift increasing to 7.1 eV on the AS surface before polishing. After polishing, the charge shift is approximately similar on both surfaces. Because of the removal of some of the conductive layer of Bi₂O₃, this decreases the conductivity of the surface increasing the charge shift to 4.8 eV on the CS surface. Also, the removal of some of the low conductive layer of SnO₂ increases the conductivity of the surface which in turn decreases the charge shift to be 5 eV on the AS surface.

4. CONCLUSIONS

XPS reveals the formation of Bi₂O₃ and SnO₂ oxides on both surfaces of Bi-Sn ribbons rapidly solidified using the melt-spinning technique. The proportion of SnO₂ on the AS surface was found to be larger than that of Bi₂O₃ on the CS surface. Also the relative amount of the total Sn to the total Bi was found to be larger on the AS side than on the CS side before and after polishing. Polishing was applied to surfaces to try to get more information about the metallic phase underneath the oxide layer. Globally, for all the surfaces in the as-received and polished samples, the atomic ratio Sn/Bi is much larger than the nominal initial value. For instance, for the nominal composition Bi-4% Sn, Sn/Bi should be (4/118.7)/(96/209) = 6.8/93.2 = 0.073, it varies between 0.9 and 3.7. This is the consequence of the relative Standard Reduction Potentials: at 25 °C, $E^{\circ}_{\text{Bi}^{3+}/\text{Bi}} = +0.308$ V, $E^{\circ}_{\text{Sn}^{2+}/\text{Sn}} = -0.14$ V and $E^{\circ}_{\text{Sn}^{4+}/\text{Sn}^{2+}} = +0.15$ V. These values mean that, thermodynamically, the tin in the presence of bismuth behaves as an anode and gets oxidized to Sn²⁺ and, eventually, to Sn⁴⁺. The charged species having higher mobility in humid media tend to easily segregate at the surface, the surface becoming very rich in (oxidized) Sn, specially in the surfaces where the oxidation conditions were more favorable. The values of the XPS charge shift on both surfaces before and after polishing are related to the high electrical conductivity of Bi₂O₃ and the low electrical conductivity of SnO₂.

ACKNOWLEDGMENTS

The authors wish to acknowledge Prof. Pedro Brogueira for AFM microscope availability. A. P. Carapeto and A. M. Botelho do Rego gratefully acknowledge the financial support provided by the Fundação para a Ciência e a Tecnologia (FCT) project RD0471-CQFM 2015-2017. A.P. Carapeto thanks FCT for PhD Grant, SFRH/BD/75734/2011. They also express their deep gratitude to Prof. Mustafa Kamal, the head of the metal physics group in physics department, Faculty of Science, Mansoura University Mansoura, Egypt.

REFERENCES

- [1] H. Jones, The status of rapid solidification of alloys in research and application, *J. Mater. Sci.* **1984**, 19, 1043.
- [2] E. W. Collings, C. E. Moblely, R. E. Maringer, H. L. Gegel, Selected Properties of Melt-Extracted Titanium-Base Polycrystalline Alloys, Rapidly Quenched Metals III, The Metals Society, England **1978**.
- [3] T. El-Ashram, Amorphous and metastable crystalline structures in rapidly solidified An-Al system using melt-spinning technique, *Eff. Defect. S.* **2004**, 159, 535.
- [4] P. Duwez, R. H. Willens, W. Klement Jr., Metastable Electron Compound in Ag-Ge Alloys *J. Appl. Phys.* **1960**, 31, 1137.
- [5] R. H. Kane, B. C. Giessen, N. J. Grant, New metastable phases in binary tin alloy systems, *Acta. Met.* **1966**, 14, 605.



- [6] R. C. Crewdson, Structure and Properties of an Amorphous Palladium Silicon Alloy, Ph.D. Thesis, California Institute of Technology, USA, **1966**.
- [7] W. Klement Jr., R. H. Willens, P. Duwez, Non-crystalline Structure in Solidified Gold–Silicon Alloys, *Nature* **1960**, 187, 869.
- [8] T. El-Ashram, M. Kamal, M. A. Raouf, S. Mosaad, Odd Valency Dopants Convert Bismuth into Semiconductor, *J. Ovonic. Res.* **2012**, 8, 97.
- [9] T. El-Ashram, Formation of Supersaturated Solid Solutions Bi-Ag and Bi-Zn by Rapid Solidification Using Melt Spinning Technique, *Mater. Sci. Appl.* **2015**, 6, 183.
- [10] A. Raouf, M. Kamal, T. El-Ashram, S. Mosaad, Rapidly Solidified Semiconducting Bi-Ag Alloys Produced Using Melt-Spinning Technique, *J. Ovonic. Res.* **2010**, 6, 297.
- [11] C. Kittel, Introduction to solid state physics, Wiley, New York **2005**.
- [12] C. A. Hoffman, J. R. Meyer, F. J. Bartoli, Semimetal-to-semiconductor transition in bismuth thin films, *Phys. Rev. B* **1993**, 48, 11431.
- [13] A. Cottrell, Theoretical Structural Metallurgy, Longmans, Green **1948**.
- [14] M. Kamal, T. El-Ashram, Zero and negative temperature coefficients of resistivity of rapidly solidified Bi-Sn alloys using melt-spinning technique, *Mater Electron.* **2008**, 19, 91.
- [15] M. Ueshima, Bi based alloy for high temperature leadfree die attach, presented at Electronic System-Integration Technology Conference (ESTC), 2012 4th, Amsterdam, Netherlands, 17-20 September, **2012**, pp. 1-5.
- [16] D. Pan, L. Zhang, J. Zhuang, W. Lu, R. Zhu, W. Qin, New application of tin–bismuth alloy for electrochemical determination of cadmium, *Mater. Lett.* **2012**, 68, 472.
- [17] A. Csanady, M. Mohai, I. Bertoti, I. Perczel, B. Albert, *Periodic Polytech-Chem* **1990**, 34, 57.
- [18] Y.-W. Kim, W. M. Griffith, F. H. Froes, Surface Oxides in P/M Aluminum Alloys, *Alloys. J. Metals* **1985**, 37, 27.
- [19] A. M. Botelho do Rego, L. F. Vieira Ferreira, Handbook of Surfaces and Interfaces of Materials, Academic Press, New York **2001**.
- [20] D. Briggs, J. T. Grant, Surface Analysis by Auger and X-ray Photoelectron Spectroscopy, IM-Publications, Chichester **2003**.
- [21] A. M. Ferraria, A. P. Carapeto, A. M. Botelho do Rego, X-ray photoelectron spectroscopy: silver salts revisited, *Vacuum* **2012**, 86, 1988.
- [22] J. C. Riviere, S. Myhra, Handbook of Surface and Interface Analysis: Methods for Problem-Solving, CRC Press, Boca Raton **2009**.
- [23] H. H. Liebermann, C. D. Graham Jr., Production of Amorphous Alloy Ribbons and Effects of Amorphous Alloy Ribbons and Effects of Apparatus Parameters on ribbon Dimensions, *IEEE Trans. Magn.* **1976**, 12, 921.
- [24] R. B. Pond, Metallic filaments and method of making same, U.S. Patent 2 825 108, **1958**.
- [25] I. Horcas, R. Fernández, J. M. Gómez-Rodríguez, J. Colchero, J. Gómez-Herrero, A. M. Baro, WSXM: A software for scanning probe microscopy and a tool for nanotechnology, *Rev. Sci. Instrum.* **2007**, 78, 013705.
- [26] R. W. M. Kwok, XPS peak fitting program for WIN95/98 XPSPEAK version 4.1., Department of Chemistry, The Chinese University of Hong Kong **2000**.
- [27] E. M. C. Fortunato, L. M. N. Pereira, Barquinha, P. M. C., A. M. Botelho do Rego, G. Gonçalves, A. Vilà, J. Morante, R. F. P. Martins, High mobility indium free amorphous oxide thin film transistors, *Appl. Phys. Lett.* **2008**, 92, 222103.
- [28] A. V. Naumkin, A. Kraut-Vass, S. W. Gaarenstroom, C. J. Powell, NIST X-ray Photoelectron Spectroscopy Database, in: NIST Standard Reference Database 20, Version 4.1. <http://srdata.nist.gov/xps>, **2012**.
- [29] A. M. Ferraria, J. D. Lopes da Silva, A. M. Botelho do Rego, XPS studies of directly fluorinated HDPE: problems and solutions, *Polymer* **2003**, 44, 7241.
- [30] S. Tanuma, C. J. Powell, D. R. Penn, Calculation of electron inelastic mean free paths (IMFP). VII. Reliability of the TPP-2M IMFP predictive equation, *Surf. Interface Anal.* **2003**, 35, 268.
- [31] M. Raposo, J. M. C. Lourenço, A. M. Botelho do Rego, A. M. Ferraria, P. A. Ribeiro, Counterions – A New Approach to Control the Degree of Ionization of Polyelectrolytes in Layer-By-Layer Films, *Colloids Surf. A* **2012**, 412, 1-10.
- [32] D. R. Lide, CRC handbook of chemistry and physics, 87th ed., CRC Press, Boca Raton **2007**.
- [33] K. S. Shamala, L. C. S. Murthy, K. N. Rao, Studies on tin oxide films prepared by electron beam evaporation and spray pyrolysis methods, *Bull. Mater. Sci.* **2004**, 27, 295.



- [34] Z. M. Jarzebski, J. P. Marton, Physical properties of SnO₂ materials II. Electrical properties, J. Electrochem. Soc. **1976**, 123, 299.
- [35] Ç. Kılıç, A. Zunger, Origins of coexistence of conductivity and transparency in SnO₂, Phys. Ver. Lett. **2002**, 88, 095501.
- [36] N. I. Anisimova, G. A. Bordovsky, V. I. Seldayev, Electrical and thermal properties of Bi₂O₃, PbO and mixed oxides of Bi₂O₃-PbO system, presented at Solid Dielectrics, 2004. ICSD 2004, 5-9 July, **2004**, pp. 141-142.
- [37] K. L. Hardee, A. J. Bard, Semiconductor electrodes X. Photoelectrochemical behavior of several polycrystalline metal oxide electrodes in aqueous solutions, J. Electrochem. Soc. **1977**, 124, 215.
- [38] L. Leontie, M. Caraman, M. Delibaş, G. I. Rusu, Optical properties of bismuth trioxide thin films, Mater. Res. Bull. **2001**, 36, 1629.
- [39] E. Öztürk, N. O. Kalaycioglu, S. Dayan, H. Ozlu, Synthesis, characterization and oxide ionic conductivity of β-type solid solution in bismuth oxide doped with ytterbium oxide binary system, Bull. Mater. Sci. **2013**, 36, 491.
- [40] M. Zarrinkhameh, A. Zendehnam, S. M. Hosseini, N. Robotmili, M. Arabzadegan, Effect of oxidation and annealing temperature on optical and structural properties of SnO₂, Bull. Mater. Sci. **2014**, 37, 533.

